First Measurement of ν_e and $\bar{\nu}_e$ Charged-Current Single Charged-Pion Production Differential Cross Sections on Argon Using the MicroBooNE Detector

P. Abratenko,[38] D. Andrade Aldana,[14] L. Arellano,[22] J. Asaadi,[37] A. Ashkenazi,[36] S. Balasubramanian,[12] B. Baller,[12] A. Barnard,[29] G. Barr,[29] D. Barrow,[29] J. Barrow,[26] V. Basque,[12] J. Bateman,[15,22] O. Benevides Rodrigues,[14] S. Berkman,[25] A. Bhat,[7] M. Bhattacharya,[12] M. Bishai,[3] A. Blake,[19] B. Bogart,[24] T. Bolton,[18] M. B. Brunetti,[17,40] L. Camilleri,[10] D. Caratelli,[4] F. Cavanna,[12] G. Cerati,[12] A. Chappell,[40] Y. Chen,[33] J. M. Conrad,[23] M. Convery,[33] L. Cooper-Troendle,[30] J. I. Crespo-Anadón,[6] R. Cross,[40] M. Del Tutto,[12] S. R. Dennis,[5] P. Detje,[5] R. Diurba,[2] Z. Djurcic,[1] K. Duffy,[29] S. Dytman,[30] B. Eberly,[35] P. Englezos,[32] A. Ereditato,[7,12] J. J. Evans,[22] C. Fang,[4] W. Foreman,[14,20] B. T. Fleming,[7] D. Franco,[7] A. P. Furmanski,[26] F. Gao,[4] D. Garcia-Gamez,[13] S. Gardiner,[12] G. Ge,[10] S. Gollapinni,[20] E. Gramellini,[22] P. Green,[29] H. Greenlee,[12] L. Gu,[19] W. Gu,[3] R. Guenette,[22] P. Guzowski,[22] L. Hagaman,[7] M. D. Handley,[5] O. Hen,[23] C. Hilgenberg,[26] G. A. Horton-Smith,[18] A. Hussain,[18] B. Irwin,[26] M. S. Ismail,[30] C. James,[12] X. Ji,[27] J. H. Jo,[3] R. A. Johnson,[8] D. Kalra,[10] G. Karagiorgi,[10] W. Ketchum,[12] M. Kirby,[3] T. Kobilarcik,[12] N. Lane,[15,22] J.-Y. Li,[11] Y. Li,[3] K. Lin,[32] B. R. Littlejohn,[14] L. Liu,[12] W. C. Louis,[20] X. Luo,[4] T. Mahmud,[19] C. Mariani,[39] J. Marshall,[40] N. Martinez,[18] D. A. Martinez Caicedo,[34] S. Martynenko,[3] A. Mastbaum,[32] I. Mawby,[19] N. McConkey,[31] L. Mellet,[25] J. Mendez,[21] J. Micallef,[23,38] A. Mogan,[9] T. Mohayai,[16] M. Mooney,[9] A. F. Moor,[5] C. D. Moore,[12] L. Mora Lepin,[22] M. M. Moudgalya,[22] S. Mulleriababu,[2] D. Naples,[30] A. Navrer-Agasson,[15] N. Nayak,[3] M. Nebot-Guinot,[11] C. Nguyen,[32] J. Nowak,[19] N. Oza,[10] O. Palamara,[12] N. Pallat,[26] V. Paolone,[30] A. Papadopoulou,[1] V. Papavassiliou,[28] H. B. Parkinson,[11] S. F. Pate,[28] N. Patel,[19] Z. Pavlovic,[12] E. Piasetzky,[36] K. Pletcher,[25] I. Pophale,[19] X. Qian,[3] J. L. Raaf,[12] V. Radeka,[3] A. Rafique,[1] M. Reggiani-Guzzo,[11] J. Rodriguez Rondon,[34] M. Rosenberg,[38] M. Ross-Lonergan,[20] I. Safa,[10] D. W. Schmitz,[7] A. Schukraft,[12] W. Seligman,[10] M. H. Shaevitz,[10] R. Sharankova,[12] J. Shi,[5] E. L. Snider,[12] S. Söldner-Rembold,[15] J. Spitz,[24] M. Stancari,[12] J. St. John,[12] T. Strauss,[12] A. M. Szelc,[11] N. Taniuchi,[5] K. Terao,[33] C. Thorpe,[22] D. Torbunov,[3] D. Totani,[4] M. Toups,[12] A. Trettin,[22] Y.-T. Tsai,[33] J. Tyler,[18] M. A. Uchida,[5] T. Usher,[33] B. Viren,[3] J. Wang,[27] M. Weber,[2] H. Wei,[21] A. J. White,[7] S. Wolbers,[12] T. Wongjirad,[38] K. Wresilo,[5] W. Wu,[30] E. Yandel,[4,20] T. Yang,[12] L. E. Yates,[12] H. W. Yu,[3] G. P. Zeller,[12] J. Zennamo,[12] and C. Zhang[3]

(MicroBooNE Collaboration)[*]

[1]*Argonne National Laboratory (ANL), Lemont, Illinois 60439, USA*
[2]*Universität Bern, Bern CH-3012, Switzerland*
[3]*Brookhaven National Laboratory (BNL), Upton, New York 11973, USA*
[4]*University of California, Santa Barbara, California 93106, USA*
[5]*University of Cambridge, Cambridge CB3 0HE, United Kingdom*
[6]*Centro de Investigaciones Energéticas, Medioambientales y Tecnológicas (CIEMAT), Madrid E-28040, Spain*
[7]*University of Chicago, Chicago, Illinois 60637, USA*
[8]*University of Cincinnati, Cincinnati, Ohio 45221, USA*
[9]*Colorado State University, Fort Collins, Colorado 80523, USA*
[10]*Columbia University, New York, New York 10027, USA*
[11]*University of Edinburgh, Edinburgh EH9 3FD, United Kingdom*
[12]*Fermi National Accelerator Laboratory (FNAL), Batavia, Illinois 60510, USA*
[13]*Universidad de Granada, Granada E-18071, Spain*
[14]*Illinois Institute of Technology (IIT), Chicago, Illinois 60616, USA*
[15]*Imperial College London, London SW7 2AZ, United Kingdom*
[16]*Indiana University, Bloomington, Indiana 47405, USA*
[17]*The University of Kansas, Lawrence, Kansas 66045, USA*
[18]*Kansas State University (KSU), Manhattan, Kansas 66506, USA*
[19]*Lancaster University, Lancaster LA1 4YW, United Kingdom*
[20]*Los Alamos National Laboratory (LANL), Los Alamos, New Mexico 87545, USA*
[21]*Louisiana State University, Baton Rouge, Louisiana 70803, USA*
[22]*The University of Manchester, Manchester M13 9PL, United Kingdom*
[23]*Massachusetts Institute of Technology (MIT), Cambridge, Massachusetts 02139, USA*
[24]*University of Michigan, Ann Arbor, Michigan 48109, USA*

[25]Michigan State University, East Lansing, Michigan 48824, USA
[26]University of Minnesota, Minneapolis, Minnesota 55455, USA
[27]Nankai University, Nankai District, Tianjin 300071, China
[28]New Mexico State University (NMSU), Las Cruces, New Mexico 88003, USA
[29]University of Oxford, Oxford OX1 3RH, United Kingdom
[30]University of Pittsburgh, Pittsburgh, Pennsylvania 15260, USA
[31]Queen Mary University of London, London E1 4NS, United Kingdom
[32]Rutgers University, Piscataway, New Jersey 08854, USA
[33]SLAC National Accelerator Laboratory, Menlo Park, California 94025, USA
[34]South Dakota School of Mines and Technology (SDSMT), Rapid City, South Dakota 57701, USA
[35]University of Southern Maine, Portland, Maine 04104, USA
[36]Tel Aviv University, Tel Aviv, Israel, 69978
[37]University of Texas, Arlington, Texas 76019, USA
[38]Tufts University, Medford, Massachusetts 02155, USA
[39]Center for Neutrino Physics, Virginia Tech, Blacksburg, Virginia 24061, USA
[40]University of Warwick, Coventry CV4 7AL, United Kingdom

(Received 1 April 2025; revised 6 June 2025; accepted 17 July 2025; published 4 August 2025)

Understanding electron neutrino interactions is crucial for measurements of neutrino oscillations and searches for new physics in neutrino experiments. We present the first measurement of the flux-averaged $\nu_e + \bar{\nu}_e$ charged-current single charged-pion production cross section on argon using the MicroBooNE detector and data from the NuMI neutrino beam. The total cross section is measured to be $[0.93 \pm 0.13(\text{stat}) \pm 0.27(\text{syst})] \times 10^{-39}$ cm^2/nucleon at a mean $\nu_e + \bar{\nu}_e$ energy of 730 MeV. Differential cross sections are also reported in electron energy, electron and pion angles, and electron-pion opening angle.

DOI: 10.1103/sfrz-c8m9

Introduction—The next generation of accelerator neutrino oscillation experiments will seek to address multiple open questions in neutrino physics through precision measurement of electron neutrino appearance in muon neutrino beams. These include the presence and scale of charge-parity violation in the neutrino sector, the neutrino mass ordering, and the resolution of anomalies observed at short baselines [1]. Several of these experiments will make use of the liquid argon time projection chamber (LArTPC) detector technology [2,3]. As such, in order to facilitate these measurements, precise understanding of ν_e interactions on argon is essential.

Cross-section modeling of ν_e interactions is typically extrapolated from ν_μ measurements. However, uncertainties on the ν_e/ν_μ interaction cross-section ratio arising from the different lepton masses and subsequent radiative corrections limit their constraining power [4–7]. Understanding these effects through measurements of ν_e interactions is crucial for precision neutrino oscillation measurements, rare-event searches, and benchmarking theoretical models used in neutrino experiments.

Reconstructing and measuring ν_e interactions also presents unique challenges compared to ν_μ interactions due to the electromagnetic cascades produced by final-state electrons. These are complicated to reconstruct and sensitive to detector calibration uncertainties. Measurements of ν_e interactions allow algorithms targeting these topologies to be evaluated and improved reducing systematic uncertainties and enhancing detector performance.

Existing measurements of ν_e cross sections on argon are limited and consist of several inclusive measurements [8–10] and a measurement without final state pions [11]. The Deep Underground Neutrino Experiment (DUNE) will be exposed to a neutrino flux peaking at energies of a few GeV [3]. At these energies, one of the dominant neutrino interaction modes leads to the excitation of baryon resonances that subsequently decay producing pions. This process has never previously been measured for ν_e interactions in argon.

This Letter presents the first measurement of the flux-averaged $\nu_e + \bar{\nu}_e$ charged-current (CC) single charged-pion production cross section on argon using MicroBooNE. The final-state topology considered consists of an electron (or positron), a single charged pion, zero neutral pions (or heavier mesons), and any number of protons or neutrons:

$$\overset{(-)}{\nu}_e + \text{Ar} \rightarrow e^{\pm} + 1\pi^{\pm} + 0\pi^0 + X, \tag{1}$$

*Contact author: microboone_info@fnal.gov

Published by the American Physical Society under the terms of the Creative Commons Attribution 4.0 International license. Further distribution of this work must maintain attribution to the author(s) and the published article's title, journal citation, and DOI. Funded by SCOAP^3.

where X represents the residual nucleus and any outgoing nucleons. These interactions will subsequently be referred to as $\overset{(-)}{\nu}_e$CC1$\pi^{\pm}$ for simplicity.

The MicroBooNE detector is an 85-metric-ton LArTPC that collected data between 2015 and 2020. It consists of an instrumented argon volume of $(2.56 \times 2.32 \times 10.36)$ m^3 (drift, vertical, and beam direction). Ionization charge produced by charged particles resulting from neutrino interactions is drifted toward three planes of readout wires, orientated vertically and at $\pm 60°$ to the vertical, by an electric field of 273 V/cm. Additionally, scintillation light is collected by an array of 32 photomultiplier tubes located behind the readout planes [12].

MicroBooNE collected data from two neutrino beams: the on-axis 8 GeV booster neutrino beam and the approximately 8° off-axis 120 GeV neutrinos at the main injector (NuMI) beam [13]. In this Letter, data from the NuMI beam operating in a mixture of forward-horn-current (FHC) neutrino mode and reverse-horn-current (RHC) antineutrino mode are used. The NuMI flux at MicroBooNE is shown for each horn-current mode in Supplemental Material [14]. The flux contains a significant fraction of $\overset{(-)}{\nu}_e$ (2.5%) due to the high beam energy and the significantly off-axis position of the detector. This makes it particularly useful for $\overset{(-)}{\nu}_e$ cross-section measurements. The average $\overset{(-)}{\nu}_e$ energies incident on MicroBooNE are 715 MeV in FHC mode and 744 MeV in RHC mode. The integrated exposure is 8.9×10^{20} protons on target (POT) in FHC mode and 11.1×10^{20} POT in RHC mode. This corresponds to the full NuMI dataset accumulated by MicroBooNE and used for the first time in this analysis.

At these neutrino energies, the dominant $\overset{(-)}{\nu}_e$ CC $1\pi^{\pm}$ production mechanism is through the $\Delta(1232)$ resonance that subsequently decays to a pion and a nucleon. In addition, there are subdominant contributions from coherent pion production and pion production as a result of deep inelastic scattering. The observed topology is also impacted by final-state interactions that can lead to pion production or absorption as the particles produced in the neutrino interaction leave the argon nucleus.

Although pion production has not previously been measured in ν_e interactions on argon, it has been probed in ν_μ interactions. ArgoNeuT has performed measurements of ν_μ- and $\bar{\nu}_\mu$-induced charged-pion production on argon [15]. MicroBooNE has performed several measurements of ν_μ-induced neutral pion production on argon for both CC [16,17] and neutral-current (NC) interactions [18,19]. This Letter presents the first measurement of $\overset{(-)}{\nu}_e$ CC $1\pi^{\pm}$ on argon. The total interaction cross section is reported along with differential cross sections in electron energy, electron and pion angles, and electron-pion opening angle. These measurements are complementary to the existing suite of $\overset{(-)}{\nu}_\mu$ measurements.

Simulation and reconstruction—The NuMI neutrino flux is simulated with Geant4 v4.10.4 [20–23] constrained with available hadron production data using the PPFX software package [24]. The integrated flux of $\overset{(-)}{\nu}_e$ with energy over 60 MeV is $1.86 \times 10^{-11}/\text{cm}^2/\text{POT}$ in FHC mode and $1.69 \times 10^{-11}/\text{cm}^2/\text{POT}$ in RHC mode. The combined FHC and RHC integrated flux is calculated by weighting the contributions from each horn-current mode according to the accumulated POT in that mode. The resulting combined integrated $\overset{(-)}{\nu}_e$ flux is $1.77 \times 10^{-11}/\text{cm}^2/\text{POT}$.

The LArSoft software framework [25] is used to perform simulation and reconstruction. Neutrino interactions are modeled using the GENIE v3.0.6 G18_10a_02_11a event generator [26] with the MicroBooNE tune applied [27]. In particular, resonant pion production is simulated using the Kuzmin-Lyubushkin-Naumov Berger-Sehgal model [28–31] and coherent pion production using the Berger-Sehgal model [32]. Propagation of the final state particles through the detector is then performed using Geant4 v4_10_3_p03c with the QGSP_BERT physics list [20–22]. This is followed by simulation of the produced ionization electrons and scintillation light and the subsequent detector response [33,34]. Simulated neutrino interactions are overlaid onto data collected while the beam is off, providing data-based modeling of cosmic-ray-induced interactions and detector noise. The Monte Carlo (MC) prediction consists of simulated neutrino interactions within the detector, simulated interactions upstream of the detector (out of cryostat), and data collected with the beam off to model beam spills where no neutrino interaction occurs.

Reconstruction is performed using the Pandora pattern-recognition toolkit. This uses a multialgorithm approach to identify neutrino interactions from cosmic-ray-induced backgrounds and to reconstruct each resulting particle. Each particle associated with the neutrino interaction is categorized as a track (muons, pions, and protons) or an electromagnetic shower (electrons and photons). A detailed description of the performance of the Pandora reconstruction in MicroBooNE can be found in Ref. [35]. Following the Pandora reconstruction, particle identification based on calorimetric and topological information [36,37] is performed. Finally, energy reconstruction is performed using particle range for tracks and through calorimetry for showers.

Signal, selection, and observables—Signal events are defined as ν_e or $\bar{\nu}_e$ CC interactions that contain an outgoing electron or positron with kinetic energy $\text{KE}_{e^{\pm}} > 30$ MeV, a single charged pion with $\text{KE}_{\pi^{\pm}} > 40$ MeV, zero neutral pions or heavier mesons, and any number of outgoing protons or neutrons. The signal definition thresholds are guided by the reconstruction thresholds for each particle type. In addition, the opening angle between the electron

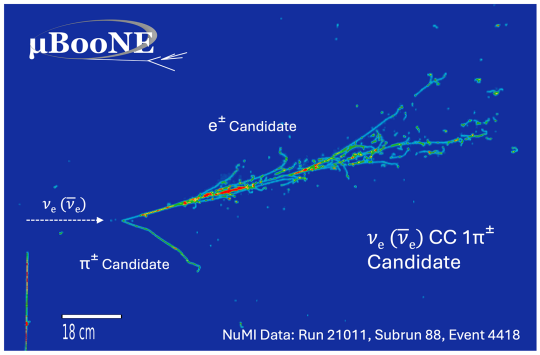


FIG. 1. Event display of a candidate $\overset{(-)}{\nu}_e$ CC $1\pi^{\pm}$ interaction.

and charged pion is required to be $\theta_{e\pi^{\pm}} < 170°$. This removes a region of phase space, containing less than 0.5% of predicted signal events, for which the reconstruction performance is poor. Figure 1 shows a candidate $\overset{(-)}{\nu}_e$ CC $1\pi^{\pm}$ interaction matching the signal definition that is selected in MicroBooNE data. A high-energy electromagnetic shower is visible along with a single track that is consistent with a charged pion.

The event selection expands upon tools developed in previous MicroBooNE $\overset{(-)}{\nu}_e$ analyses [9–11,38,39]. Charged-current $\overset{(-)}{\nu}_e$ interactions are first identified through the presence of an electromagnetic shower consistent with an electron. Tracks present in the event are then assumed to have originated from either protons or charged pions. These are distinguished based on their differing ionization profiles or the presence of pion reinteractions. The focus on first identifying charged-current $\overset{(-)}{\nu}_e$ interactions avoids the need to distinguish between final-state muons and charged pions that are otherwise more challenging to separate.

Well-reconstructed candidate events are first identified that have at least one electromagnetic shower and at least one track contained within the instrumented volume. Next, a set of simple cuts are used to remove obvious background events. Cosmic-ray-induced interactions are rejected through Pandora classification based on topological characteristics. Electromagnetic showers resulting from neutral pion decays to photons are rejected by applying cuts on three features: the fraction of energy in the leading shower compared to all showers; the shower start position relative to the interaction vertex; and the transverse spread of the shower. Finally, $\overset{(-)}{\nu}_e$ interactions containing protons but not pions (referred to subsequently as $\overset{(-)}{\nu}_e$ CC Np) are rejected by requiring at least one track has an ionization profile (dE/dx) that is inconsistent with a stopping proton Bragg peak hypothesis [40].

After these initial cuts, more sophisticated methods are applied to refine the event selection further focusing on background suppression through the use of two boosted decision trees (BDTs) trained with XGBoost [41]. The BDTs are trained separately for FHC and RHC modes accounting for differences in neutrino composition and energies.

The first BDT focuses on the shower information to distinguish between electrons and photons from neutral pion backgrounds ($\overset{(-)}{\nu}_e$ CC π^0, $\overset{(-)}{\nu}_\mu$ CC π^0, and NC π^0). It uses both calorimetric and topological information about the primary shower, any secondary showers if present, and any showerlike clusters of charge identified close to the neutrino interaction.

The second BDT focuses on the track information and aims to distinguish between charged pions and protons, in particular, targeting remaining $\overset{(-)}{\nu}_e$ CC Np interactions where the proton does not have a clear Bragg peak and, hence, is not rejected at the previous stage. This BDT uses the dE/dx of the track compared to different particle hypotheses along with topological information focusing on the ends of tracks to identify pion reinteractions or decays. Interactions are selected where only one track is identified as a charged-pion candidate, with any number of additional proton candidates allowed.

Figure 2 shows the distribution of scores for the π^0-rejection BDT and $\overset{(-)}{\nu}_e$ CC Np-rejection BDT compared with data. The $\overset{(-)}{\nu}_e$ CC Np-rejection BDT is shown after the cut on the π^0-rejection BDT has been applied. Both are shown for FHC mode; RHC mode can be found in Supplemental Material [14]. Both BDTs achieve good signal-background separation for their target topologies. For the π^0 rejection, 99.2% of π^0-induced photon showers are removed while keeping 42.0% of $\overset{(-)}{\nu}_e$-induced electron showers. For the $\overset{(-)}{\nu}_e$ CC Np rejection, 94.3% of $\overset{(-)}{\nu}_e$ CC Np interactions are rejected while keeping 67.1% of $\overset{(-)}{\nu}_e$ CC $\pi^{\pm}$ interactions. In addition, excellent data-MC agreement within statistical and systematic uncertainties is seen across the full BDT score distributions. A full description of the BDT input variables along with data-MC comparisons used can be found in Supplemental Material [14].

Candidate $\overset{(-)}{\nu}_e$ CC $\pi^{\pm}$ interactions are selected with efficiencies of 6.2% and 5.8% and purities of 57.3% and 58.5% for the FHC and RHC beam periods, respectively. Further details on the selection performance can be found in Supplemental Material [14]. In total, 116 candidate events pass the selection in the combined 2.0×10^{21} POT data sample. The selected signal events are predicted to be 78% ν_e interactions and 22% $\bar{\nu}_e$ interactions. They are dominated by resonant production (85%), with smaller contributions from deep-inelastic scattering (11%), quasielastic interactions (2%), and coherent interactions (2%).

The observables considered are the total rate; the electron energy E_e; the electron and pion angles θ_e and θ_π, respectively, with respect to the neutrino direction; and

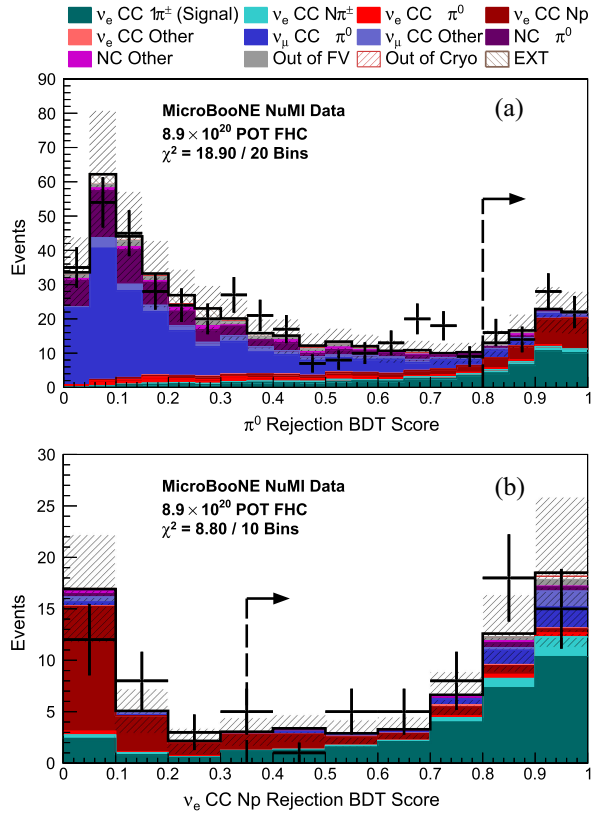


FIG. 2. Distribution of scores for (a) the π^0-rejection BDT and (b) the $\overset{(-)}{\nu}_e$ CC Np-rejection BDT compared with FHC mode data. The shaded band shows the systematic and statistical uncertainty on the MC prediction, and the black points show the data with statistical uncertainties. The dashed lines show the cuts applied, where events to the right are selected.

the electron-pion opening angle $\theta_{e\pi}$. Since MicroBooNE is off axis to the NuMI beam, the exact neutrino direction is not known in data. To reconstruct angles relative to the neutrino direction, neutrinos are assumed to be produced at the NuMI target position. This gives an effective approximation of the neutrino direction with 95% of signal events having an approximated direction within 3° of the true direction. In simulation, the true direction is known, and, hence, the smearing arising from this approximation can be accounted for during unfolding [10]. Details on the performance of this approximation can be found in Supplemental Material [14]. The reconstruction resolution is approximately 17% for E_e, 10% for θ_e, 10% for θ_π, and 9% for $\theta_{e\pi}$.

Each observable is binned such that there are five bins with approximately ten expected signal events each. In the case of E_e, the highest energy bin also serves as an overflow bin. For each observable, good data-MC agreement is observed within uncertainties. The selected event distributions can be found in Supplemental Material [14].

The largest backgrounds are interactions producing neutral pions (13.0% of passing events) and $\overset{(-)}{\nu}_e$ CC Np interactions (11.7% of passing events). Two sidebands are constructed to assess the agreement between data and simulation for these backgrounds. A π^0-rich sideband is constructed by reversing the π^0-rejection BDT cut. This results in a sample with 68.8% purity of π^0-containing interactions with a mixture of $\overset{(-)}{\nu}_e$ CC π^0, $\overset{(-)}{\nu}_\mu$ CC π^0, and NC π^0 topologies. A $\overset{(-)}{\nu}_e$ CC Np-rich sideband is constructed by reversing both the $\overset{(-)}{\nu}_e$ CC Np-rejection BDT cut and the proton Bragg peak cut. This results in a sample with 77.6% purity of $\overset{(-)}{\nu}_e$ CC Np interactions. The level of agreement with data is assessed across each observable considered for both sidebands. Good data-MC agreement is seen across all distributions, indicating the background modeling is sufficient to proceed with cross-section extraction. The sideband selected event distributions can be found in Supplemental Material [14].

Cross-section extraction and uncertainties—The flux-averaged total cross section and differential cross sections as a function of true kinematic variables are reported. The cross sections are extracted using the Wiener singular value decomposition unfolding technique [42] using a first-derivative regularization term. The impact of the regularization is encoded in a regularization matrix that can be applied to generator predictions to allow direct comparison with the extracted cross sections in the regularized truth space. A blockwise approach to unfolding is used, allowing correlations between bins in different variables to be evaluated and reported [43].

Uncertainties on the extracted cross sections are assessed from a variety of sources. The statistical and systematic uncertainties are encoded in a covariance matrix using a blockwise formalism [43]. The total covariance matrix is constructed by summing the covariance matrices of each individual uncertainty.

Systematic uncertainties are considered on the neutrino flux from hadron production and beam-line geometry modeling [23,24]; the neutrino interaction cross-section modeling with GENIE [27]; secondary particle reinteractions [44]; detector response modeling including the scintillation light yield, recombination model, space charge effects [45], and ionization signal response [46]; out-of-cryostat interaction modeling; the number of argon targets; and POT counting. In the unfolded results, the dominant systematic uncertainty arises from the neutrino flux modeling (∼20%–30%) due to the challenges in simulating the 8° off-axis NuMI beam. This is followed by detector response modeling (∼15%), predominantly from recombination modeling due to the reliance on calorimetric variables to identify charged pions; and cross-section modeling (∼10%). The other sources of systematic uncertainty are subdominant.

Statistical uncertainties on the data and simulation are evaluated using Poisson uncertainties. Data statistical

TABLE I. Extracted total cross section compared with predictions from generators.

Generator	σ [10^{-39} cm^2/nucleon]	χ^2/n_{bins}
Unfolded data	$0.93 \pm 0.13(\text{stat}) \pm 0.27(\text{syst})$	
NuWro 21.09.2	0.76	0.30/1
NEUT 5.4.0.1	0.83	0.11/1
GiBUU 2025	0.74	0.42/1
GENIE 3.4.0 AR23	0.62	1.11/1
GENIE 3.6.0 G18 μB	0.68	0.68/1

uncertainties are subdominant for the total cross-section measurement at around 10% but are comparable with systematic uncertainties or dominant for the differential cross-section measurements at around 30%. The total covariance and correlation matrices are reported in Supplemental Material [14].

The robustness of the unfolding procedure and regularization is assessed using fake data produced by the GENIE and NuWro 19.02.2 [47] generator models. These fake-data tests motivated expanding the cross-section modeling uncertainty by treating the NuWro sample as an additional systematic universe [48].

Results—The extracted total cross section is shown in Table I, and differential cross sections in E_e, θ_e, θ_π, and $\theta_{e\pi}$ are shown in Fig. 3. The differential cross sections are presented in regularized truth space described by the regularization matrix available in Supplemental Material [14]. The unfolded data are compared with generator predictions from NuWro 21.09.2 [47], NEUT 5.4.0.1 [49], GiBUU 2025 [50], GENIE 3.0.6 G18_10a_02_11a MicroBooNE tune [27] (labeled GENIE 3.0.6 G18μB), and GENIE 3.4.2 AR23_20i_00_000 [26] (labeled GENIE 3.4.2 AR23). Resonant pion production is simulated using the Kuzmin-Lyubushkin-Naumov Berger-Sehgal model [28–31] in GENIE, the Adler-Rarita-Schwinger formalism [51] in NuWro, and the Rein-Sehgal model in NEUT [52]. Coherent pion production is simulated with the Berger-Sehgal [32] model in GENIE, NuWro, and NEUT. GiBUU models resonant pion production following the MAID analysis [53] and does not simulate coherent pion production.

The total cross section is measured to be $[0.93 \pm 0.13(\text{stat}) \pm 0.27(\text{syst})] \times 10^{-39}$ cm^2/nucleon. This is consistent with the predictions from each of the generators considered. The data slightly prefer the higher cross sections predicted by NEUT, NuWro, and GiBUU compared with the lower cross sections predicted by GENIE. This could suggest a slight preference for the treatment of resonant pion production or nuclear medium effects in these models. However, the sensitivity of the measurement is limited by the large systematic uncertainties on the flux modeling.

The extracted differential cross sections in E_e, θ_e, θ_π, and $\theta_{e\pi}$ are all consistent with the generator predictions. The preference for higher cross sections results in lower χ^2 for NEUT, NuWro, and GiBUU in E_e, θ_e, and $\theta_{e\pi}$, whereas these models have a higher χ^2 for θ_π, hinting at possible shape disagreement in this variable. The smallest χ^2 are seen for E_e where there is minimal shape difference between the

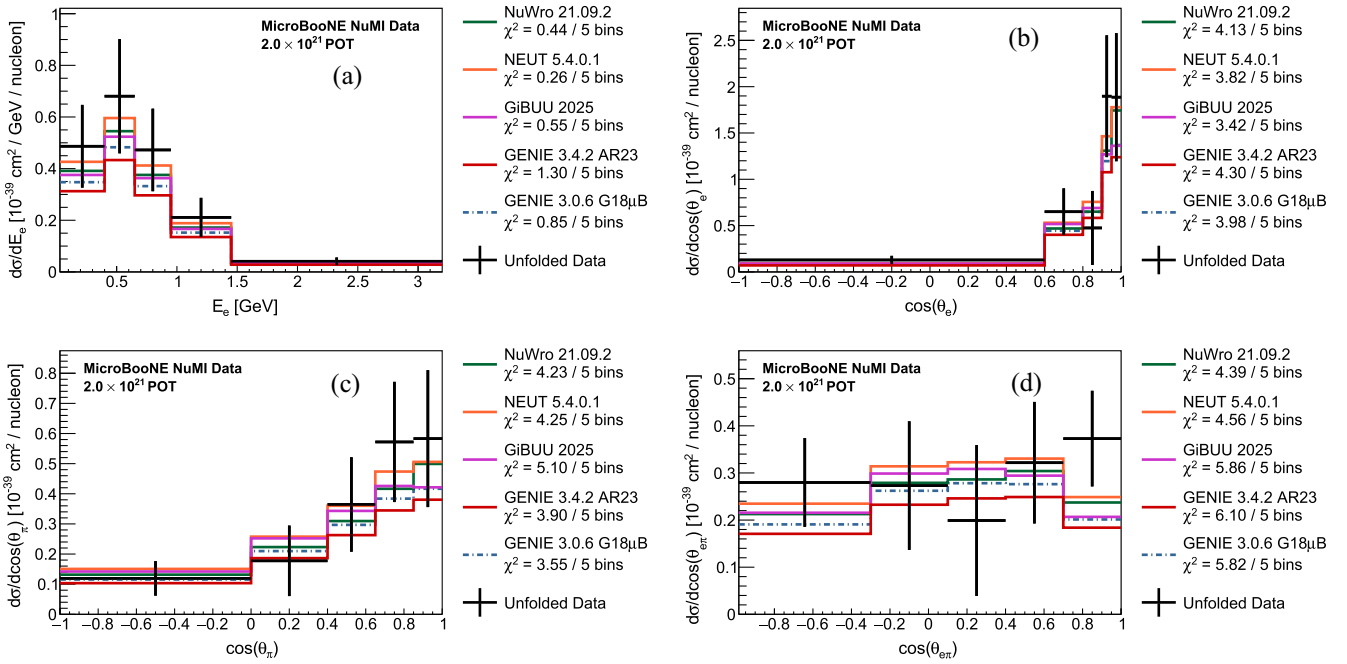


FIG. 3. Extracted differential cross sections in (a) electron energy, (b) electron angle, (c) pion angle, and (d) electron-pion opening angle compared with generator predictions. The unfolded data points show both statistical and systematic uncertainties.

data and the generator predictions. The largest χ^2 are seen for $\theta_{e\pi}$ driven by the smallest opening angle bin where, in particular, GENIE and GiBUU underpredict the cross section. However, due to the large statistical and flux uncertainties, all models lie within or close to 1σ of the data, suggesting, in general, good modeling of this process within the sensitivity of this measurement. To achieve greater model separation, future measurements would require greater statistics, potentially through improved reconstruction, and improved flux modeling. In particular, additional hadron production data to constrain the off-axis NuMI flux could significantly reduce the associated uncertainties.

Conclusions—We have presented the first measurement of the flux-averaged $\overset{(-)}{\nu}_e$ charged-current single charged-pion production cross section on argon using the MicroBooNE detector. The full NuMI beam dataset accumulated by MicroBooNE is used for the first time corresponding to a total exposure of 2.0×10^{21} POT with mean $\overset{(-)}{\nu}_e$ energy of 730 MeV. The total cross section is measured to be $[0.93 \pm 0.13(\text{stat}) \pm 0.27(\text{syst})] \times 10^{-39}\ \text{cm}^2/\text{nucleon}$. Differential cross sections are also reported as functions of electron energy, the electron and pion angles with respect to the neutrino direction, and the electron-pion opening angle. These are found to be in good agreement with generator predictions within uncertainties. This is the first measurement of pion production in $\overset{(-)}{\nu}_e$ interactions on argon, one of the dominant interaction modes at the energies of the DUNE neutrino flux. It is essential to understand this process in order to facilitate the DUNE physics program, and direct measurements will have a critical impact to motivate modeling improvements. While this is the first time this process has been measured, the measurement is limited by statistical uncertainties and the challenges arising from the off-axis flux; future experiments in the SBN program [2] and the DUNE near detector [54] are expected to be able to improve on this.

Acknowledgments—This document was prepared by the MicroBooNE Collaboration using the resources of the Fermi National Accelerator Laboratory (Fermilab), a U.S. Department of Energy, Office of Science, Office of High Energy Physics (HEP) User Facility. Fermilab is managed by Fermi Forward Discovery Group, LLC, acting under Contract No. 89243024CSC000002. MicroBooNE is supported by the following: the U.S. Department of Energy, Office of Science, Offices of High Energy Physics and Nuclear Physics; the U.S. National Science Foundation (NSF); the Swiss National Science Foundation; the Science and Technology Facilities Council (STFC), part of the United Kingdom Research and Innovation; the Royal Society (United Kingdom); the United Kingdom Research and Innovation (UKRI) Future Leaders Fellowship; and the NSF AI Institute for Artificial Intelligence and Fundamental Interactions. Additional support for the laser calibration system and cosmic ray tagger was provided by the Albert Einstein Center for Fundamental Physics, Bern, Switzerland. We also acknowledge the contributions of technical and scientific staff to the design, construction, and operation of the MicroBooNE detector as well as the contributions of past collaborators to the development of MicroBooNE analyses, without whom this work would not have been possible.

Data availability—The data that support the findings of this Letter are not publicly available. The data are available from the authors upon reasonable request.

[1] M. Sajjad Athar *et al.*, Status and perspectives of neutrino physics, Prog. Part. Nucl. Phys. **124**, 103947 (2022).
[2] P. Machado, O. Palamara, and D. W. Schmitz, The short-baseline neutrino program at Fermilab, Annu. Rev. Nucl. Part. Sci. **69**, 363 (2019).
[3] B. Abi *et al.* (DUNE Collaboration), Long-baseline neutrino oscillation physics potential of the DUNE experiment, Eur. Phys. J. C **80**, 978 (2020).
[4] M. Day and K. S. McFarland, Differences in quasi-elastic cross-sections of muon and electron neutrinos, Phys. Rev. D **86**, 053003 (2012).
[5] M. Martini, N. Jachowicz, M. Ericson, V. Pandey, T. Van Cuyck, and N. Van Dessel, Electron-neutrino scattering off nuclei from two different theoretical perspectives, Phys. Rev. C **94**, 015501 (2016).
[6] A. Nikolakopoulos, N. Jachowicz, N. Van Dessel, K. Niewczas, R. González-Jiménez, J. M. Udías, and V. Pandey, Electron versus muon neutrino induced cross sections in charged current quasielastic processes, Phys. Rev. Lett. **123**, 052501 (2019).
[7] O. Tomalak, Q. Chen, R. J. Hill, and K. S. McFarland, QED radiative corrections for accelerator neutrinos, Nat. Commun. **13**, 5286 (2022).
[8] R. Acciarri *et al.* (ArgoNeuT Collaboration), First measurement of electron neutrino scattering cross section on argon, Phys. Rev. D **102**, 011101(R) (2020).
[9] P. Abratenko *et al.* (MicroBooNE Collaboration), Measurement of the flux-averaged inclusive charged-current electron neutrino and antineutrino cross section on argon using the NuMI beam and the MicroBooNE detector, Phys. Rev. D **104**, 052002 (2021).
[10] P. Abratenko *et al.* (MicroBooNE Collaboration), First measurement of inclusive electron-neutrino and antineutrino charged current differential cross sections in charged lepton energy on argon in MicroBooNE, Phys. Rev. D **105**, L051102 (2022).
[11] P. Abratenko *et al.* (MicroBooNE Collaboration), Differential cross section measurement of charged current ν_e interactions without pions in MicroBooNE, Phys. Rev. D **106**, L051102 (2022).
[12] R. Acciarri *et al.* (MicroBooNE Collaboration), Design and construction of the MicroBooNE detector, J. Instrum. **12**, P02017 (2017).
[13] P. Adamson *et al.*, The NuMI neutrino beam, Nucl. Instrum. Methods Phys. Res., Sect. A **806**, 279 (2016).

[14] See Supplemental Material at http://link.aps.org/supplemental/10.1103/sfrz-c8m9 for details on the NuMI flux at MicroBooNE, description of the BDT input variables, reverse-horn-current mode data BDT score distributions, a breakdown of the selection performance, the performance of the reconstructed neutrino direction approximation, the signal region and sideband selected distributions, the unfolded differential cross-section covariance, correlation and regularization matrices, and the tabulated results.

[15] R. Acciarri *et al.* (ArgoNeuT Collaboration), First measurement of the cross section for ν_μ and $\bar{\nu}_\mu$ induced single charged pion production on argon using ArgoNeuT, Phys. Rev. D **98**, 052002 (2018).

[16] C. Adams *et al.* (MicroBooNE Collaboration), First measurement of ν_μ charged-current π^0 production on argon with the MicroBooNE detector, Phys. Rev. D **99**, 091102 (2019).

[17] P. Abratenko *et al.* (MicroBooNE Collaboration), Measurement of the differential cross section for neutral pion production in charged-current muon neutrino interactions on argon with the MicroBooNE detector, Phys. Rev. D **110**, 092014 (2024).

[18] P. Abratenko *et al.* (MicroBooNE Collaboration), Measurement of neutral current single π^0 production on argon with the MicroBooNE detector, Phys. Rev. D **107**, 012004 (2023).

[19] P. Abratenko *et al.* (MicroBooNE Collaboration), First double-differential cross section measurement of neutral-current π^0 production in neutrino-argon scattering in the MicroBooNE detector, Phys. Rev. Lett. **134**, 161802 (2025).

[20] S. Agostinelli *et al.*, Geant4—A simulation toolkit, Nucl. Instrum. Methods Phys. Res., Sect. A **506**, 250 (2003).

[21] J. Allison *et al.*, Geant4 developments and applications, IEEE Trans. Nucl. Sci. **53**, 270 (2006).

[22] J. Allison *et al.*, Recent developments in Geant4, Nucl. Instrum. Methods Phys. Res., Sect. A **835**, 186 (2016).

[23] P. Abratenko *et al.* (MicroBooNE Collaboration), Updates to the NuMI flux simulation at MicroBooNE, Report No. MICROBOONE-NOTE-1129-PUB, 2024.

[24] L. Aliaga *et al.* (MINERvA Collaboration), Neutrino flux predictions for the NuMI beam, Phys. Rev. D **94**, 092005 (2016); **95**, 039903(A) (2017).

[25] E. Snider and G. Petrillo, LArSoft: Toolkit for simulation, reconstruction and analysis of liquid argon TPC neutrino detectors, J. Phys. Conf. Ser. **898**, 042057 (2017).

[26] C. Andreopoulos *et al.*, The GENIE neutrino Monte Carlo generator, Nucl. Instrum. Methods Phys. Res., Sect. A **614**, 87 (2010).

[27] P. Abratenko *et al.* (MicroBooNE Collaboration), New $CC0\pi$ GENIE model tune for MicroBooNE, Phys. Rev. D **105**, 072001 (2022).

[28] J. A. Nowak (MiniBooNE Collaboration), Four momentum transfer discrepancy in the charged current π^+ production in the MiniBooNE: Data vs. theory, AIP Conf. Proc. **1189**, 243 (2009).

[29] K. S. Kuzmin, V. V. Lyubushkin, and V. A. Naumov, Lepton polarization in neutrino nucleon interactions, Mod. Phys. Lett. A **19**, 2815 (2004).

[30] C. Berger and L. Sehgal, Lepton mass effects in single pion production by neutrinos, Phys. Rev. D **76**, 113004 (2007).

[31] K. M. Graczyk and J. T. Sobczyk, Form factors in the quark resonance model, Phys. Rev. D **77**, 053001 (2008); **79**, 079903(E) (2009).

[32] C. Berger and L. M. Sehgal, Partially conserved axial vector current and coherent pion production by low energy neutrinos, Phys. Rev. D **79**, 053003 (2009).

[33] C. Adams *et al.* (MicroBooNE Collaboration), Ionization electron signal processing in single phase LArTPCs. Part I. Algorithm description and quantitative evaluation with MicroBooNE simulation, J. Instrum. **13**, P07006 (2018).

[34] C. Adams *et al.* (MicroBooNE Collaboration), Ionization electron signal processing in single phase LArTPCs. Part II. Data/simulation comparison and performance in MicroBooNE, J. Instrum. **13**, P07007 (2018).

[35] R. Acciarri *et al.* (MicroBooNE Collaboration), The Pandora multi-algorithm approach to automated pattern recognition of cosmic-ray muon and neutrino events in the MicroBooNE detector, Eur. Phys. J. C **78**, 82 (2018).

[36] C. Adams *et al.* (MicroBooNE Collaboration), Calibration of the charge and energy loss per unit length of the MicroBooNE liquid argon time projection chamber using muons and protons, J. Instrum. **15**, P03022 (2020).

[37] C. Adams *et al.* (MicroBooNE Collaboration), Reconstruction and measurement of $\mathcal{O}(100)$ MeV energy electromagnetic activity from $\pi^0 \to \gamma\gamma$ decays in the MicroBooNE LArTPC, J. Instrum. **15**, P02007 (2020).

[38] P. Abratenko *et al.* (MicroBooNE Collaboration), Search for an anomalous excess of charged-current ν_e interactions without pions in the final state with the MicroBooNE experiment, Phys. Rev. D **105**, 112004 (2022).

[39] P. Abratenko *et al.* (MicroBooNE Collaboration), Search for an anomalous production of charged-current ν_e interactions without visible pions across multiple kinematic observables in MicroBooNE, arXiv:2412.14407.

[40] P. Abratenko *et al.* (MicroBooNE Collaboration), Calorimetric classification of track-like signatures in liquid argon TPCs using MicroBooNE data, J. High Energy Phys. 12 (2021) 153.

[41] T. Chen and C. Guestrin, XGBoost: A scalable tree boosting system, in *Proceedings of the 22nd ACM SIGKDD International Conference on Knowledge Discovery and Data Mining* (Association for Computing Machinery, New York, 2016), pp. 785–794.

[42] W. Tang, X. Li, X. Qian, H. Wei, and C. Zhang, Data unfolding with Wiener-SVD method, J. Instrum. **12**, P10002 (2017).

[43] S. Gardiner, Mathematical methods for neutrino cross-section extraction, arXiv:2401.04065.

[44] J. Calcutt, C. Thorpe, K. Mahn, and L. Fields, Geant4Reweight: A framework for evaluating and propagating hadronic interaction uncertainties in Geant4, J. Instrum. **16**, P08042 (2021).

[45] P. Abratenko *et al.* (MicroBooNE Collaboration), Measurement of space charge effects in the MicroBooNE LArTPC using cosmic muons, J. Instrum. **15**, P12037 (2020).

[46] P. Abratenko *et al.* (MicroBooNE Collaboration), Novel approach for evaluating detector-related uncertainties in a LArTPC using MicroBooNE data, Eur. Phys. J. C **82**, 454 (2022).

[47] T. Golan, C. Juszczak, and J. T. Sobczyk, Final state interactions effects in neutrino-nucleus interactions, Phys. Rev. C **86**, 015505 (2012).

[48] P. Abratenko *et al.* (MicroBooNE Collaboration), Multi-differential cross section measurements of ν_μ-argon quasielasticlike reactions with the MicroBooNE detector, Phys. Rev. D **108**, 053002 (2023).

[49] Y. Hayato and L. Pickering, The NEUT neutrino interaction simulation program library, Eur. Phys. J. Special Topics **230**, 4469 (2021).

[50] O. Buss, T. Gaitanos, K. Gallmeister, H. van Hees, M. Kaskulov, O. Lalakulich, A. B. Larionov, T. Leitner, J. Weil, and U. Mosel, Transport-theoretical description of nuclear reactions, Phys. Rep. **512**, 1 (2012).

[51] K. M. Graczyk, D. Kielczewska, P. Przewlocki, and J. T. Sobczyk, C_5^A axial form factor from bubble chamber experiments, Phys. Rev. D **80**, 093001 (2009).

[52] D. Rein and L. M. Sehgal, Neutrino excitation of baryon resonances and single pion production, Ann. Phys. (N.Y.) **133**, 79 (1981).

[53] U. Mosel, Neutrino event generators: Foundation, status and future, J. Phys. G **46**, 113001 (2019).

[54] A. Abed Abud *et al.* (DUNE Collaboration), Deep underground neutrino experiment (DUNE) near detector conceptual design report, Instruments **5**, 31 (2021).